DIPARTIMENTO DI INGEGNERIA DELL'INFORMAZIONE

CORSO DI LAUREA MAGISTRALE IN
ICT FOR INTERNET AND MULTIMEDIA

"Crystallization of amorphous Ta2O5 coatings for gravitational waves astronomy"

Relatore: Prof. Marco Bazzan

Laureando: Diego Alonso Diaz Riega

Correlatore: Dott. Valeria Milotti

ANNO ACCADEMICO 2024 – 2025

Data di laurea 04/12/2024

Abstract

In 1915, Albert Einstein published his theory of General Relativity, proposing the existence of ripples in space-time, known as Gravitational waves. It was not until 2015 when the U.S. National Science Foundation Laser Interferometer Gravitational-wave Observatory (NSF LIGO) detected for the first time, a gravitational wave. A Gravitational wave detector works similarly to a Michelson interferometer with two mirrors in each arm operating as a Fabry-Perot cavity, increasing the effective distance light travels and, in consequence, improving its sensitivity. These mirrors are composed of alternating layers of amorphous materials with different refractive index. Mirror coatings play a key role in the overall performance of the GW detector, since the most-sensitive frequency range of the interferometers lies between 40-400 Hz, same band where the coating Brownian thermal noise (CTN) sets up a limit in the detector. Thermal annealing has been proven as a way to reduce CTN. However, this treatment also induces the generation of crystals in the material, increasing its optical scattering. The aim of this thesis is to characterize and analyze the optical properties of tantalum oxide Ta_2O_5 coatings, manufactured using Ion Beam Sputtering Deposition technique and later treated in an oven at high temperatures for step-increasing hours, where a crystalization process takes place. Finally, given the changes of crystallization, the evolution of its properties are studied. A visual analysis is carried out using Atomic Force Microscopy (AFM) and Optical Microscopy, estimating surface roughness (RMS) and Grain Size Distribution (GSD) respectively. These examinations revealed the formation of single-crystalline grains of random orientations with a trend of increasing surface roughness and average crystal sizes. The optical scattering measurement was done using a home-build scatterometer device. Results demonstrated that at high crystallization levels, optical scattering increased.

Science, my lad, is made up of mistakes, but they are mistakes which it is useful to make, because they lead little by little to the truth.

— Jules Verne, A Journey to the Center of the Earth

Contents

Bibliography

List of Figures

Chapter 1

Physics of Gravitational Waves

In 1687, Newton formulated the law of universal gravitation in his book *Philosophiae Naturalis Principia Mathematica*[1], proposing that a body attracts every other body in the universe, with a gravitational force between them, proportional to the product of their masses and inversely proportional to the square of the distance between them. The gravitational force is always attractive with an infinite range and its experienced instantaneously at a distance.

Later, in 1905, Poincaré suggested the existence of gravitational waves (GW) by modifying Newton's law in his article *On the Dynamics of the Electron*[2]. It concluded that all the forces had an electromagnetic origin and, as a consequence, gravity propagates at the speed of light. Nevertheless, this theory did not explain the anomalies observed regarding the perihelion of Mercury. It was not until 1915 that Einstein[3] presented a unified explanation of gravity as a geometric property of space and time known as General Relativity (GR). Similarly to Poincaré[2], this theory led to the prediction of the existence of GW (which are comparable but not equal to electromagnetic waves), propagating through space-time at the speed of light.

Einstein's GWs are coherent emissions from bulk motions of energy, producing distortions of space-time with practically no absorption or scattering detectable at frequency $f < 10^4 Hz$. In contrast to electromagnetic (EM) waves, which are oscillating fields propagating through space-time and created as a result of an incoherent superposition of waves from molecules, atoms, and particles, with a typical frequency of detection of $f > 10^7 Hz$[4].

Astrophysically, given their energy and distance of the source, the GW can be considered to be in the weak field regime, hence, their propagation (and other properties) can be analyzed accordingly[5].

It took until the 14 September 2015, a century later since it was theorized, that the first GW was detected in two LIGO (Laser Interferometer Gravitational wave Observatory) stations separated by a distance of 1900 km. This event opened a new window of observation of the universe, and a new era in astronomy [6]. Since then, multiple GW were detected [7] and other facilities

became online: VIRGO (Pisa, Italy) and KAGRA (Kamioka Gravitational Wave Detector), located in Japan.

1.1 General Relativity and Gravitational Waves

Gravitation its the manifestation of the curvature of spacetime. Since gravity appears when there is matter, there must be a relationship between curvature of spacetime and the distribution of matter. This is exactly what Einstein's Field Equations (EFE) represent. They connect a curvature tensor to a tensor of matter distribution. However, there are conditions that must be fullfilled. First, all the equations should be written in tensorial form, so that they hold in all coordinate systems. Secondly, Einstein's theory must reduce to Newton's theory to a very good approximation in the limit of weak fields and slow motion of sources (non relativistic motion) [5]. The EFE are given below:

$$G_{\mu\nu} = \frac{8\pi G}{c^4} T_{\mu\nu} \tag{1.1}$$

$$G_{\mu\nu} = R_{\mu\nu} - \frac{1}{2} R g_{\mu\nu} \tag{1.2}$$

Where $G_{\mu\nu}$ is the Einstein's tensor, representing the curvature of spacetime and $T_{\mu\nu}$ is an energy/momentum tensor with vanishing divergence, G is Newton's constant of gravitation. Einstein's tensor is written in terms of the Ricci tensor $R_{\mu\nu}$ and a Ricci scalar R with a metric tensor $g_{\mu\nu}$. The last two terms are necessary since $R_{\mu\nu}$ does not have a vanishing divergence by itself.

The EFE are second order coupled nonlinear partial differential equations for the metric components $g_{\mu\nu}$. Since the Riemann tensor involves the second order derivatives of the metric, the equations are also of second order. They are also nonlinear as they involve products of $g_{\mu\nu}$ and their first and second order derivatives with respect to the coordinates. The physical meaning of this is that a gravitational field also produces a gravitational field since it carries energy. On the contrary, Newton's equation is linear and so also are the Maxwell's equations of electromagnetism. The implication is that in GR we cannot superimpose solutions as we could do in Newton's theory of gravitation and in Maxwell's electromagnetism. This makes solutions hard to obtain. In practice , symmetry conditions are exploited so that the problem becomes treatable [5].

1.1.1   Linearized EFE

It is possible to rewrite the metric tensor $g_{\alpha\beta}$ in a nearly Cartesian system as a small perturbation $h_{\alpha\beta}$ around a flat spacetime Minkowski metric $\eta_{\alpha\beta}$:

$$g_{\alpha\beta} = \eta_{\alpha\beta} + h_{\alpha\beta} \tag{1.3}$$

$$\eta_{\alpha\beta} = g_{\alpha\beta} = \begin{bmatrix} -1 & 0 & 0 & 0 \\ 0 & 1 & 0 & 0 \\ 0 & 0 & 1 & 0 \\ 0 & 0 & 0 & 1 \end{bmatrix} \tag{1.4}$$

With a small perturbation term $|h_{\alpha\beta}| << 1$, and, from an astrophysical point of view, this value is typically found to be $h_{\alpha\beta} \approx 10^{-22}$ or less when the waves reach our detectors, justifying in keeping only the first order terms of $h_{\alpha\beta}$.

To linearize the Ricci tensor from EFE under the weak field limit, the product of the gamma elements is ignored as they are second and higher order. The expression in $g_{\alpha\beta}$ is replaced by h because η_{jk} are constants values whose derivatives are zero. We use four indices $(\alpha, \beta, \mu, \nu)$ to represent time and space coordinates

$$R_{\alpha\beta\mu\nu} = \frac{1}{2}(g_{\alpha\nu,\mu\beta} + g_{\mu\beta,\alpha\nu} - g_{\alpha\beta,\mu\nu} - g_{\mu\nu,\alpha\beta}) + \Gamma^2 \tag{1.5}$$

$$R_{\alpha\beta\mu\nu} \approx \frac{1}{2}(h_{\alpha\nu,\mu\beta} + h_{\mu\beta,\alpha\nu} - h_{\alpha\beta,\mu\nu} - h_{\mu\nu,\alpha\beta}) \tag{1.6}$$

To further reduce this, in the transverse traceless gauge, the field equations become a wave equation

$$(\nabla^2 - \frac{1}{c^2}\frac{\partial^2}{\partial t^2})h_{\mu\nu} = 0 \tag{1.7}$$

with plane waves as a solution with two polarizations at $45°$ between components[4]

$$h_{\mu\nu} = a\hat{h}_+(t - \frac{z}{c}) + b\hat{h}_x(t - \frac{z}{c}) \tag{1.8}$$

The first term of gravitational radiation is quadrupolar and its strength depends on the magnitude of this non axisymmetric moment. The largest term for gravitational radiation is

$$h_{\mu\nu} = \frac{2G}{Rc^4}I_{\mu\nu} \tag{1.9}$$

Where G stands for Newton's constant, R is the distance of the source of GW (accelerating body)

3
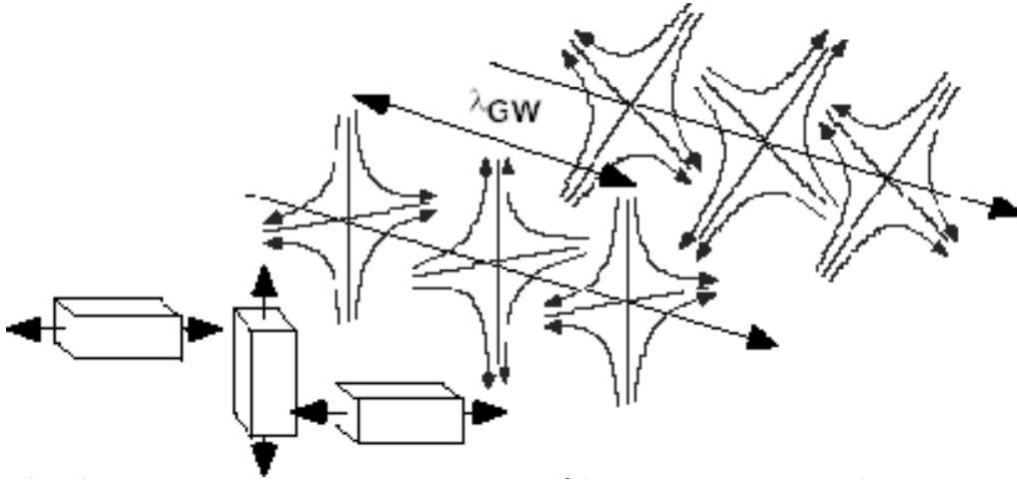
Figure 1.1: The passage of GW distorts the space-time producing a change in length in two orthogonal directions oscillating with the GW frequency.

and $I_{\mu\nu}$ is the reduced quadrupole moment tensor[4].

1.2 Detection of Gravitational Waves

A first attempt to detect GW was presented by Webber in a paper outlining his thoughts on this topic in 1960 [21]. In essence, he suggested using vibration measurements from a mechanical system to identify GW. In order to achieve this, Weber created a sizable metal cylinder that he used as a kind of "antenna" weighting 1.5 tones. The main idea is to monitor resonance vibrations that would be eventually, "activated" by a gravitational wave pulse transit and detect this motion with crystals close to the cylinder. The crystal is a piezoelectric sensor that converts a mechanical vibration into an electrical impulse. The system was placed in an isolated environment and cooled down to reduce molecular vibrations. However, after many years of upgrades and improvements to the cylinder system. Some detections were measured, nonetheless they were later confirmed as not generated from gravitational waves. Subsequently, an interferometer was proposed [6].

1.2.1 Interferometer

The first explicit suggestion of a laser interferometer detector was outlined in the former USSR by Gertsenshtein and Pustovoid in 1962 [8]. A basic schematic is presented in Figure 1.2.

The process begins with a laser emitting a beam of monochromatic light that hits the beam splitter. This surface is partially reflective, so there is a 50% chance of light get transmitted

Figure 1.2: Basic schematic of an interferometer for detecting GW.

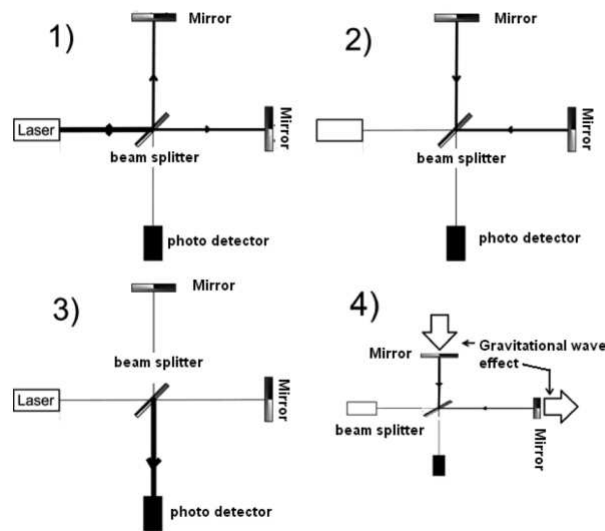through to the mirror at the right side of the diagram and 50% of it reflected to the mirror at the upper side of the sketch. Both beams recombine when they meet at the beam splitter and the resulting beam is reflected toward the detector. Finally, the photodetector measures the light intensity of the recombined beam. This intensity is proportional to the square of the height of the recombined wave. At initial conditions, the reflective mirrors are in a fixed position with distance L from the beam splitter with an stable intensity measured in the photodetector. When a gravitational wave event is ocurring, the distance of one reflective mirror from the beamsplitter should increase by a distance Δl, while the other decrease, changing the intensity measured by the photodetector compared to the initial fixed condition.

A key specific feature of the interferometer detection effectiveness is given by the length of its arms. This is the distance "L" between the wave splitter and its mirrors. The wavelength of the gravitational wave sets the size of the detector L needed. It is known that the optimal size of the arms are 1/4 of the wavelength of the GW to be detected. For a gravitational wave with frequency of 100 Hz, this implies that L should be 750 km, which is actually too long to make except by folding the beams back and forth using the Fabry–Pérot technique, reaching the desired optimal size. In practice, it is of importance to have an interferometer with very long arms matching the frequencies one plans to observe. The importance of a long arm "l" is easy to explain if we introduce the definition of the dimensionless amplitude $h = \Delta l / L$. If a gravitational wave produces a displacement Δl for the distance between the mirrors, according to the definition of h, the resulting change Δl will be greater the longer the interferometer arm L is, since they are directly proportional ($\Delta l = L \times h$)[6].

1.2.2 LIGO

The LIGO detectors are Michelson interferometers whose mirrors also serve as gravitational test masses. The Michelson arm lengths are long 4 km long and 1.2 m diameter stainless steel tubes that supports a vacuum system. Each arm contains a resonant Fabry–Perot optical cavity made up of a partially transmitting input mirror and a high reflecting end mirror (test masses). The cavities cause the light to effectively bounce back and forth multiple times in the arms, increasing the carrier power and phase shift for a given strain amplitude. In the LIGO detectors the Fabry–Perot cavities multiply the signal by a factor of 100 for a 100 Hz GW. The laser source is a diode-pumped, Nd : YAG, and emits 10 W in a single frequency at 1064 nm. The interferometer optics, including the test masses, are fused-silica substrates with multilayer dielectric coatings, manufactured to have extremely low scatter and low absorption. The test masses substrates are polished so that the surface deviation from a spherical figure, over the central 80 mm diameter, is typically 5 Å or smaller, and the surface microroughness is typically less than 2 Å. The mirror coatings are made using ion-beam sputtering, a technique known for producing ultralow-loss mirrors. The absorption level in the coatings is generally a few parts-permillion (ppm) or less, and the total scattering loss from a mirror surface is estimated to be 60–70 ppm. At full power operation, a total of 20–60 mW of light is absorbed in the substrate and in the mirror surface of each input test mass, depending on their specific absorption levels[9].

Figure 1.3: Aerial photograph of the LIGO observatory at Hanford, Washington. The laser and optic is contained in the large corner buildings, where beam tubes extend for 4 km in each direction. The tubes are covered by the arched, concrete enclosures. Image from [9]

1.2.3 Advanced Virgo

Advanced Virgo, located in Cascina (IT), is a laser interferometer, and its working principle is the destructive interference pattern of a Michelson interferometer. The Injection system consists of a main laser beam generated by a 1064 nm Nd:YAG laser source; such laser is pre-stabilized in both amplitude and frequency before actually being injected inside the interferometer. Then, the laser beam is sent into a triangular resonant cavity, the Input Mode Cleaner (IMC), which serves the purpose of both cleaning the laser field from high order modes, in order to inject as much as possible in the interferometer only the TEM00 fundamental mode. Following this, the laser beam is injected in the main interferometer. The main interferometer (central and right part of Figure 1.5) is composed by the seven main optics which form this enhanced Michelson configuration; in the middle, the Beam Splitter (BS) mirror splits the incoming light and sends it in the two arms of the interferometer. Differently from the standard Michelson interferometer, in Virgo the arms (North and West) are not composed by a single reflecting mirror at the end of each arm, but rather by a resonant Fabry-Pérot 3 km long cavity made by two highly reflective mirrors, with the reflecting sides facing one another. Since the interferometer working point is dark fringe, this means that most of the light, once reflected by the arms and recombined by the BS mirror, is sent back toward the Injection system; therefore, a semi-reflective mirror is added between the Injection system and the Fabry-Pérot Michelson, in order to create with the latter another resonant cavity: this Power Recycling (PR) mirror reflects this rejected light back into the main interferometer, effectively increasing the circulating power of the laser field in the detector [10].

The Fabry-Pérot cavity are made of large cylinders of ultra-pure fused silica (Suprasil™3002 and 312), with a diameter of 350 mm, a thickness of 200 mm, and a weight of 42 kg. This kind of material is highly transparent to 1064 nm laser light (absorption is less than 0.3 ppm/cm for Suprasil™3002). Reflectivity is assured by a coating film of titania doped tantala ($TiO2:Ta2O5$) applied to the mirror surfaces by ion beam sputtering (IBS), made by a stack of alternate layers of two materials with different refractive indexes, forming a Bragg reflector.[10].

Figure 1.4: Aerial view of the Virgo detector (image credit: The Virgo Collaboration).
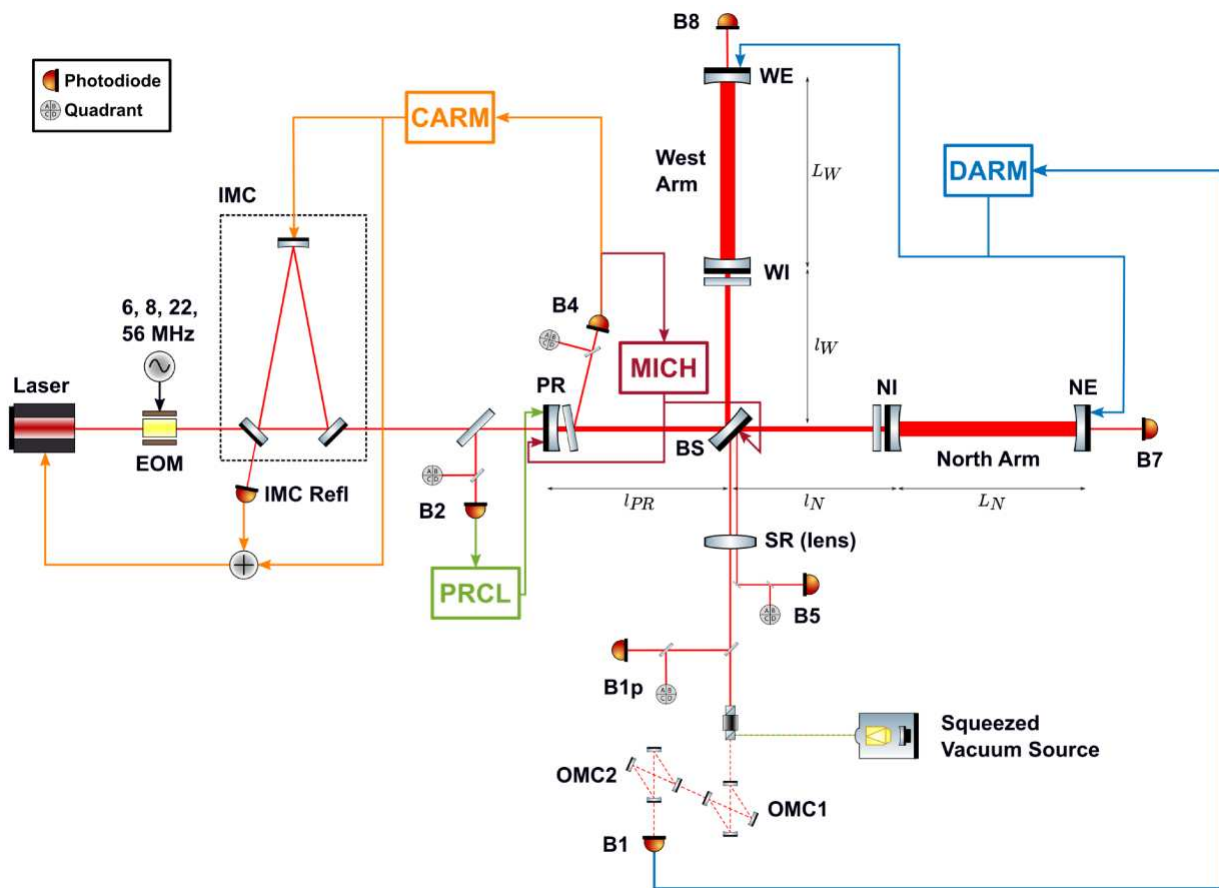
Figure 1.5: Optical layout of Advanced Virgo. Image from [10].
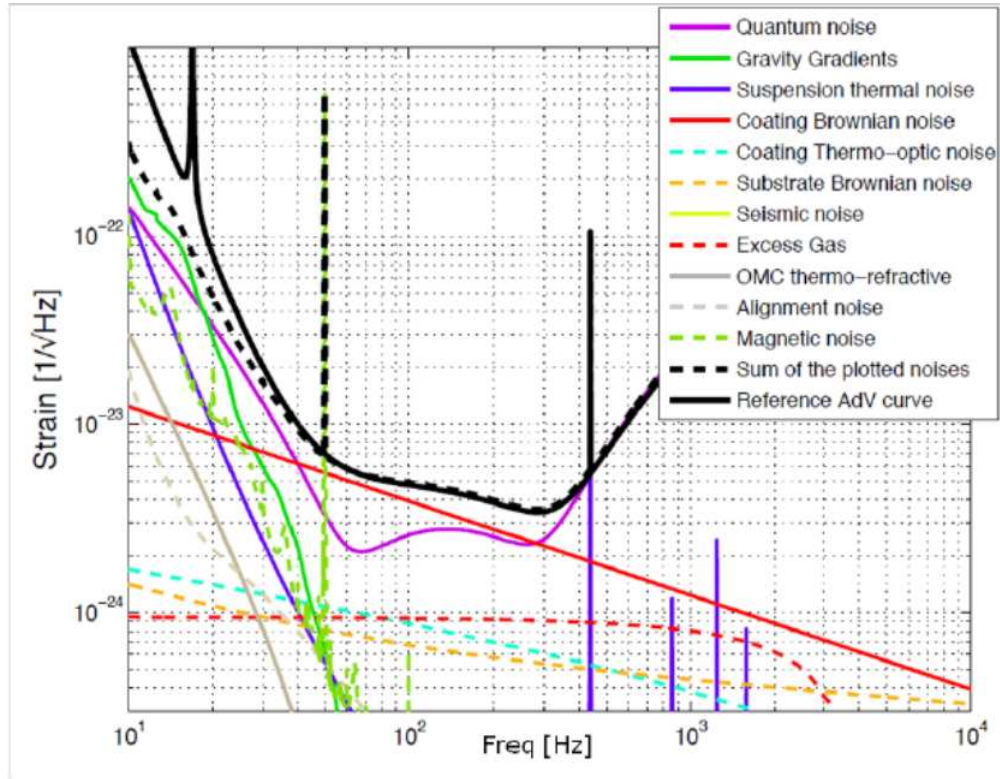
1.3   Sensitivity of Advanced Virgo

Figure 1.6: Advanced Virgo strain sensitivity with the main noise sources limiting at different frequency ranges. Image from [11]

At the frequency band of 30 Hz to 300 Hz, the detector sensitivity is limited by the thermal noise of the coating layers of the core mirror surfaces. It can be shown [10][9] that the thermal noise is related to the mechanical loss angle of the materials under consideration, so the lower the loss angle, the lower the amount of thermal noise introduced by a given element. Advanced Virgo and Advanced LIGO core mirrors are large cylinders of ultra-pure fused silica. This kind of material is highly transparent to 1064 nm laser light, and also exhibits an extremely low value of the loss angle ($\varphi \approx 10{-}9$ rad), which is necessary to reduce the thermal noise contribution to the interferometer sensitivity budget, as it will be explained below. The ultra-fine polishing of the mirror surfaces achieves sub-nanometric roughness, reducing scattered light between cavities. Reflectivity is assured by a coating film applied to the mirror surfaces by IBS. Coating power absorption is lower than 1 ppm, and the reflectivity of the end mirror is 99.999%. For the mirrors, the coating loss angle is much larger than the substrate one, hence, even if the energy stored in the thick substrate is larger, coating is responsible for most of the energy losses, and consequently for the resulting thermal noise. For advanced detectors, silica is used as low refractive index material, whereas titania doped tantala is used as high refractive

index material. A post-deposition thermal treatment (annealing) for a time duration of 10 h at 500 °C is done after coating deposition to lower optical absorption and internal stress, improving also the mechanical properties of the coating reducing the loss angles of the whole stack. After annealing, IBS deposed silica shows a mechanical loss angle of 2.2 10−5 rad at 60 Hz, which is about three to four order of magnitude larger than the silica bulk loss, but still considerably smaller than the loss angle of tantala (2.8 10−4 rad at 60 Hz). Doping tantala with titania (with a ratio Ti/Ta = 0.27) decreases the loss angle of about 25% (2.2 10−4 at 60 Hz), still ten times above the silica one. This makes the mid-frequency sensitivity of current detectors limited by the thermal noise of the high refractive index layers of coating. By means of an optimization process a tuning of the coating layers on the stack has been done in order to ensure the right value of reflectivity using the minimum total thickness of high index layers.

1.4   Distributed Bragg reflector

A distributed Bragg reflector (DBR) is a an alternating multi-layer structure of high and low refractive indices n_h and n_l , which are typically wavelength dependent. The wavelength range with high reflectivity, called the stop band, results from constructive interference of light reflecting on multiple interfaces. For high reflectivity around a central wavelength λc for perpendicular incidence, the layer thicknesses should be $d_i = \lambda_c/4n_i$, with n_i the corresponding refractive index [12]. In this case, the peak reflectivity is given by :

$$R_{HR,max} = (\frac{1 - (\frac{n_s}{n_a})(\frac{n_h}{n_l})^{2N}}{1 + (\frac{n_s}{n_a})(\frac{n_h}{n_l})^{2N}})^2 \qquad (1.10)$$

Where n_s is the refractive index of the substrate, n_a that of the surrounding ambient , and N is the number of repeated pairs of high and low refractive index layers. In this way a peak reflectivity exceeding 99% can be achieved for a specific wavelength[12].

The working principle of this type of reflector can be understood as follows. Each boundary between the two materials contributes a Fresnel reflection. For the design wavelength, the optical path length difference between reflections from subsequent interfaces is half the wavelength; in addition, the amplitude reflection coefficients for the interfaces have alternating signs. Therefore, all reflected components from the interfaces interfere constructively, resulting in a strong reflection. The reflectivity achieved is determined by the number of layer pairs and by the refractive index contrast between the low and high refractive index of the materials. The reflection bandwidth is determined mainly by the refractive index contrast; if is too small, even using a very large number of coating layers will not work[13].

Figure 1.7 shows the reflectance and the group delay dispersion as functions of the wave-
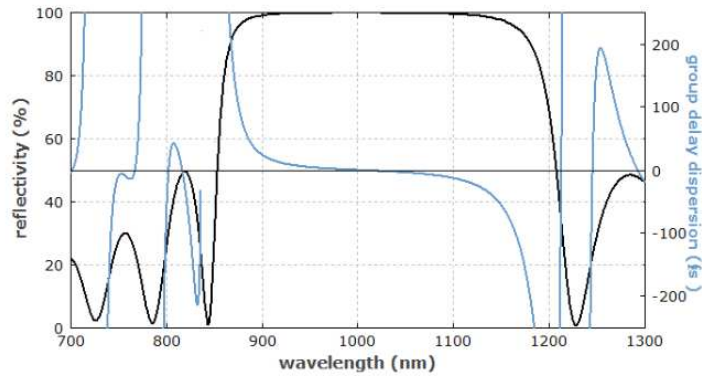
Figure 1.7: Reflectance (black curve) and chromatic dispersion (blue curve) of a theoretical 8 layer titanium oxide - silicon dioxide mirror. Figure taken from [13].

length. The reflectance is high over some optical bandwidth, which depends on the refractive index contrast of the materials used and on the number of layer pairs. The dispersion is calculated from the second derivative of the reflection phase with respect to the optical frequency. It is small near the center of the reflection band, but grows rapidly near the edges [13].

1.5   Ion beam sputtering

Ion Beam Sputtering (IBS), is a deposition method used in the production of thin-films in which an ion source is used to sputter the coating material from a target, which can be metallic or dielectric. An IBS system is typically composed of an ion source, a target (coating to sputter), and a substrate. Figure 1.8 illustrates the basic setup of the IBS process and illustrate an advanced ion beam source incorporating an electron gun. In this setup, an ion beam strikes the surface of the target, generating free ions, which can be either ionic or neutral. These particles then evaporate and are deposited onto the substrate positioned above the target.

1. The ion beam of Ar gas is produced by applying high voltage between two electrodes at the cathode and anode: The cathode electrode the source material (target is attached) whereas at anode the substrate is housed.

2. Then the ion beam (Ar^+) is focused on a target material, and

3. The sputtered species (cations, anions or neutral particles) cool down during flying around the vacuum chamber and deposit onto a substrate to create either a metallic or dielectric film. 4. It may be desirable to heat the substrates (with an electric heater) during deposition to improve overall performance.

The advantage of using ion beam sputtering is because the ion beam is monoenergetic (ions possess the equal energy) and highly collimated, enabling an extremely precise thickness control and deposition of very dense, high quality films as compared to other PVD (physical vapor
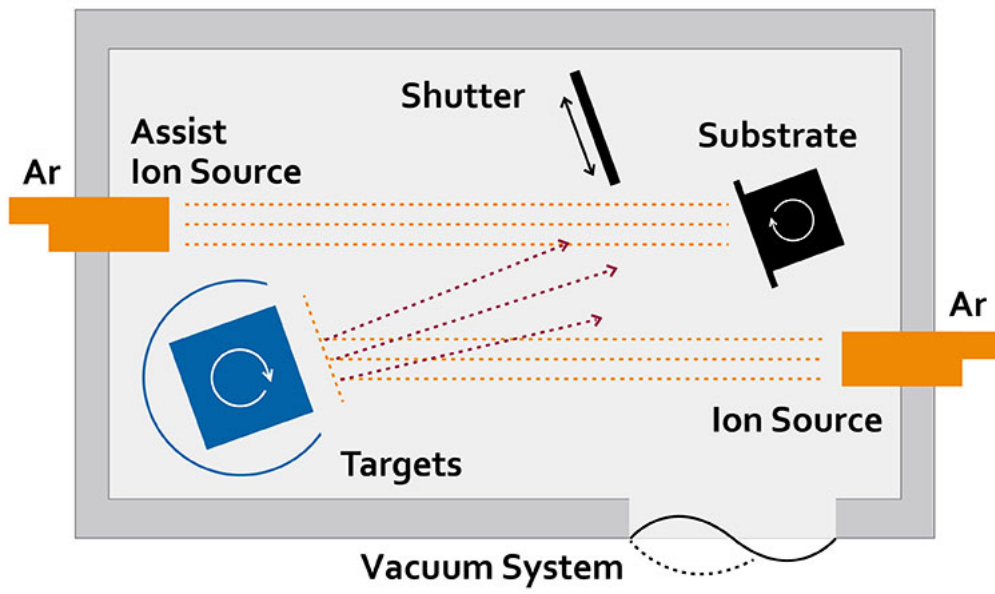
11

deposition) technologies[14].

Figure 1.8: Basic schematic of the Ion Beam Sputtering process.

Chapter 2

Optical Scattering

Light scattering is the physical phenomenon involving the deviation of electromagnetic waves (EM) from a straight trajectory by irregularities or inhomogeneities within a material. In the context of coatings and thin films for gravitational waves (GW) detectors, light scattering is of particular importance, as it directly impacts the performance of the whole system.

The objective of this thesis is to measure the physical (surface roughness) and scattering changes that tantalum oxide coatings undergoes when exposed to thermal treatments with respect to time. The root mean square average (RMS) is used characterize the microscopic irregularities of the coating surface, while bidirectional reflectance distribution function (BRDF) and total integrated scattering (TIS) is employed to describe scattering. Before expanding these concepts, some relevant radiometric quantities and concepts are explained below.

(a) **Flux or power:** The flux, or power, of a source is equal the number of photons/second (ph/s) it emits. This quantity is represented by the Greek symbol Φ. The flux of a source can be a function of many variables, such as position, direction, wavelength, and polarization. This quantity is also expressed in Watts (W), which can be computed from photons per second:

$$Watts = \sum_{i=1}^{n} \frac{hc}{\lambda_i}.\Phi_i \tag{2.1}$$

where n is the number of photons, h is Planck's constant (6.626×10^{-34} Joule·s), c is the speed of light (3×108 meters/s), and i is the wavelength (in meters) of the ith photon[15].

(b) **Exitance:** Exitance M is equal to the flux per unit area emitted by a source, defined as

$$M = \frac{d\Phi}{dA} \tag{2.2}$$

where $d\Phi$ is the differential flux emitted by the source, and dA is the differential area of the source. Exitance is specified in ph/s-unit area. Using photometric units, exitance is given in lux (lm/m^2).

For a Lambertian surface, which reflects light equally into all directions, the exitance of the surface is related to its radiance L as[15]:

$$M = \Phi L \tag{2.3}$$

(c) **Radiance:** The radiance of a source L is equal to

$$L = \frac{d^2\Phi}{dA\cos\theta d\omega} \tag{2.4}$$

where $d\Phi$ is the differential power emitted by the differential projected area of the source $dA cos(\theta)$ into the differential solid angle $d\omega$, as shown in Fig. 2.1.

Radiance is used to quantify the amount of light of a surface: the more flux a surface emits per unit area or the more flux it emits per projected solid angle, the greater its radiancen[15].
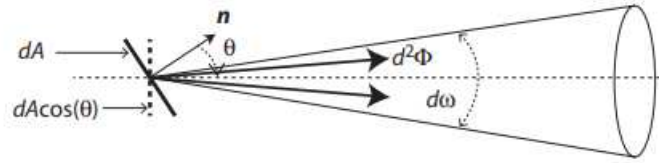
Figure 2.1: Quantities used in the definition of radiance. Image from [15]

(d) **Reflectance, transmittance, and absorption :** Reflectance ρ is the amount of flux reflected by a surface, normalized by the amount of flux incident on it. Transmittance τ is the amount of flux transmitted by a surface, normalized by the amount of flux incident on it. Any flux not reflected or transmitted is absorbed (α). Conservation of energy requires thatn[15]:

$$\rho + \tau + \alpha = 1 \tag{2.5}$$

2.1 Bidirectional Scattering Distribution Function

The bidirectional scattering distribution function (BSDF) is the radiance of a scattering surface, normalized by the irradiance incident of the surface:

$$BSDF(\theta_i, \Phi_i, \theta_s, \Phi_s) = \frac{dL(\theta_i, \Phi_i, \theta_s, \Phi_s)}{dE(\theta_i, \Phi_i)} \tag{2.6}$$

where θ_i and Φ_i are the elevation and azimuth angles of the incident ray; while θ_s and Φ_i are the elevation and azimuth angles of the scattered ray (as as shown in Fig in Fig. 2.2), dL is the differential radiance of the scattering surface, and dE is the differential incident irradiance. Equation (2.6) can also be written in terms of the differential scattered flux per differential projected solid angle $d\Phi_s/d\Omega_s$, normalized by the differential incident flux $d\Phi_i$ as:

$$BSDF = \frac{d\Phi_s/d\Omega_s}{(d\Phi_i)\cos\theta_s} \tag{2.7}$$

The units of BSDF are $1/sr$. Another quantity is the cosine-corrected BSDF (also called the scatter function), which is equal to $BSDF \times cos\theta_s$.

The BSDF is a generalized term that includes light scattered in all directions. In contrast, Bidirectional Reflectance Distribution Function (BRDF) specifically characterizes only the reflective component of scattering, describing how much light is reflected in a particular outgoing direction as a function of the incoming light direction. Mathematically, BRDF is a subset of the BSDF, focusing exclusively on reflective behavior and ignoring any transmission through the material.

In this thesis, BRDF is used for the study of coatings because it specifically focuses on the reflection component of light scattering, which is most relevant for analyzing surface properties such as roughness, reflectivity, and uniformity without considering transmitted or absorbed light, which are typically negligible or not of interest in reflective coating evaluations.
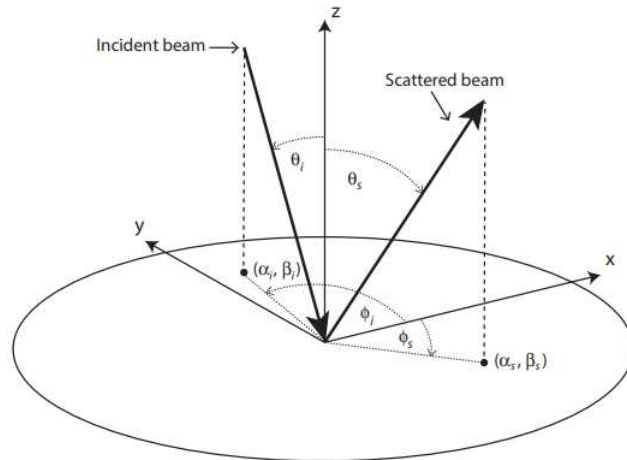

Figure 2.2: Angles used for the definition of BRDF. Image from [15].

2.2 Total Integrated Scattering

Total Integrated Scattering (TIS) is the ratio of total power scattered by a surface in the reflected or transmitted direction to the power incident on it, which is equal to the integral of the BSDF over the projected solid angle of the hemisphere:

$$TIS = \int_0^{2\pi} \int_0^{\pi/2} BSDF \sin\theta_s \cos\theta_s d\theta_s d\omega \tag{2.8}$$

In order for energy to be conserved, the TIS of any BRDF (whether measured or modeled) is at most 1, as it represents the fraction of incident light scattered by a surface integrated over all angles. Since TIS quantifies the amount of light scattered out of the incident beam, it cannot exceed 100% of the incident light. In other words, the total amount of light scattered by a surface, summed over all directions of reflections, cannot surpass the total amount of incident light. Thus, by definition, TIS is a dimensionless quantity bounded by the value 1. An example of a material with a TIS of 1 is a Lambertian surface [15].

According to [16] it is possible to relate RMS roughness σ and the wavelength λ of incident light (in this case, the wavelength of the laser used as source of light). Assuming $\sigma << \lambda$, the TIS ratio is written as:

$$TIS \approx (\frac{4\pi\sigma\cos\theta_0}{\lambda})^2 \tag{2.9}$$

Or rewritten in terms of surface RMS roughness σ:

$$\sigma \approx \frac{\lambda}{4\pi\cos\theta_0}\sqrt{TIS} \tag{2.10}$$

Chapter 3

Experimental methods

3.1   Production of Tantala Samples

The tantalum oxide coating used for this research were deposited on a silicon substrate using Ion Beam sputtering technique. These samples were manufactured and supplied by the same laboratory in charge of creating the mirrors for the VIRGO and LIGO interferometers, Laboratoire des Matériaux Avancés (LMA)[18], located in France. For the IBS process, the energy and current of the Argon sputtering ions were 1.25 keV and 0.6 A, respectively, with an average coating deposition rate of 2.85 ± 0.04 $nm\ s^{-1}$. The total pressure during the coating process was of the order of 10^{-4} mbar, with 21 sccm of Ar and 37 sccm of O_2 injected into the chamber, producing a 500nm thick layer of tantalum oxide on top of a 75 mm diameter, 0.5 mm thick, single-side-polished, (100) p-doped silicon wafer[19].

After the deposition process, all the samples were pretreated at 500°C for 10h [20]. In this step no cristallization was detected.

Subsequent annealing steps were performed in the laboratories of the University of Padova using 3 models of tubular furnaces: Carbolite Gero D-7542, Carbolite Gero 30-3000, and Carbolite CTF 12/75/700. A calibration of temperature and spatial uniformity was carried out with a thermocouple to detect the optimal positions inside the ovens, as the temperature varies inside in the range of cm. Samples where placed in a quartz vessel as it withstands high temperatures[20].

For each step, the temperature inside the oven was increased at a rate of 100°C per hour, until it reaches 630°C. This is done because, without the small temperature increments, cracks would show up on the surface. Based on multiple tests, a temperature of 630°C was found to be an ideal value to have a controlled growth of crystals in the tantalum oxide coating ,hence , it was the constant temperature selected to be used in subsequent and incremental annealing steps

(as detailed in Table 3.1) to create a group of samples K1–K5 to analyze[19].

Sample	Step 0	Step 1	Step 2	Step 3	Step 4	Step 5
As deposited	-	-	-	-	-	-
K0	10 h, 500 °C	-	-	-	-	-
K1	10 h, 500 °C	6 h, 630 °C	-	-	-	-
K2	10 h, 500 °C	6 h, 630 °C	3 h, 630 °C	-	-	-
K3	10 h, 500 °C	6 h, 630 °C	3 h, 630 °C	3 h, 630 °C	-	-
K4	10 h, 500 °C	6 h, 630 °C	3 h, 630 °C	3 h, 630 °C	3 h, 630 °C	-
K5	10 h, 500 °C	6 h, 630 °C	3 h, 630 °C	3 h, 630 °C	3 h, 630 °C	3 h, 630 °C

Table 3.1: Annealing times of the samples.

3.2 Optical Microscopy

Optical microscopy is an important instrument for analyzing coatings after thermal treatment, especially in understanding the transformations in Grain Size Distribution (GSD). During thermal processing, coatings often experience grain growth, which can significantly impact the material's properties, such as surface roughness and scattering. By investigating the GSD, optical microscopy allows us to observe how grains develop or evolve under different thermal conditions [21].

Figure 3.1: Microscope Keyence VHX-7000 used in this research.

For this thesis, I used a Keyence VHX-7000 digital microscope, located in a clean room. Each sample was illuminated using coaxial lighting, with two polarizing filters placed in the

optical path. Rotating the relative positions of the polarizers allows us to find a different response in the image generated, enhancing the contrast and taking advantage of the interaction of polarized light with birefringent materials that may be present in the sample. Images with 2500x magnification were taken. Figure 3.2 presents two images captured from the same area of sample K5, using two different position of the polarizers. In both pictures, the background remains uniform, exhibiting a consistent surface color in this region regardless of the polarization state. Nevertheless, grains within the film exhibit perceptible color changes between the two polarizations. This variation implies that the grains possess anisotropic optical effects. The observed phenomenon highlights the grains response to polarization, likely due to their orientation, structure, or material changes after the annealing process.

Software included in the microscope was utilized to analyze the microstructure of tantalum pentoxide coatings, allowing for the recognition of optically inhomogeneous grains. This method provided valuable insights into the influences of thermal treatment on the structural evolution of Ta_2O_5 by estimating both the size and number of grains, providing data for assessing the degree of crystallization in the samples. Samples were annealed at different time intervals, and the software facilitated the identification of changes in grain structure as a function of annealing time.
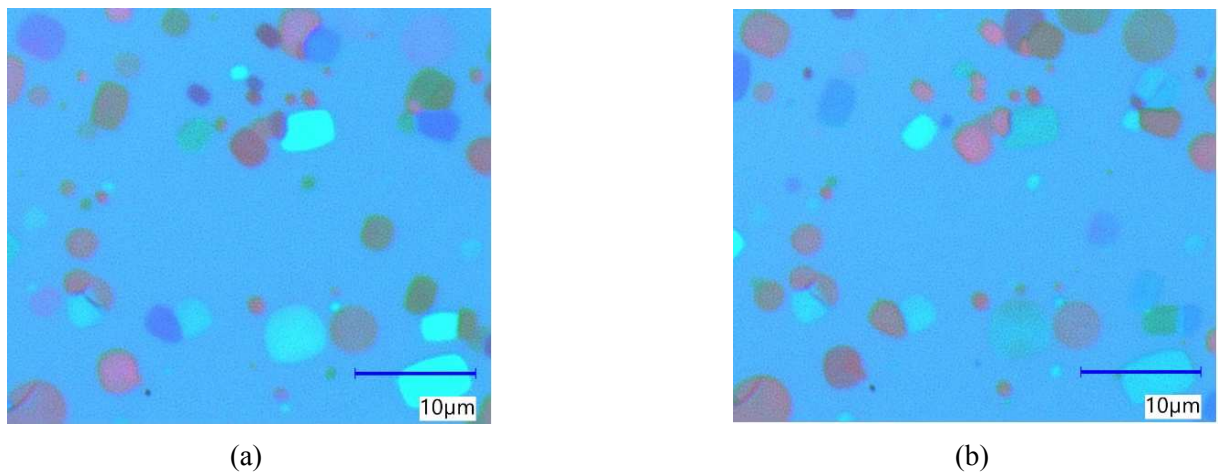

(a)   (b)

Figure 3.2: Microscopic images of sample K5 taken in the same area using two different polarizations.

3.3   Scatterometer

The Bidirectional reflectance distribution function (BRDF) was estimated by using a scatterometer (Figure 3.5) located in a ISO-8 clean room at the University of Padova. The scatterometer consists of a light source (in this research a laser), a sample holder (Figure 3.4), mirrors, and photodiodes (which depends on the laser wavelengths). Samples are supported by a holder, while

the laser beam source is directed towards them. Then, the reflected and transmitted light are captured with a high sensitivity photodetector that rotates around the sample at a radius of ≈ 30, cm measuring the scattered light at small angular intervals [17]. Depending on the laser power used, a filter might be attached to the photodetector to avoid saturation. At the moment of my intership, two laser sources of 532 nm and 1064 nm were avalaible. A schematic representation of the device is provided below.
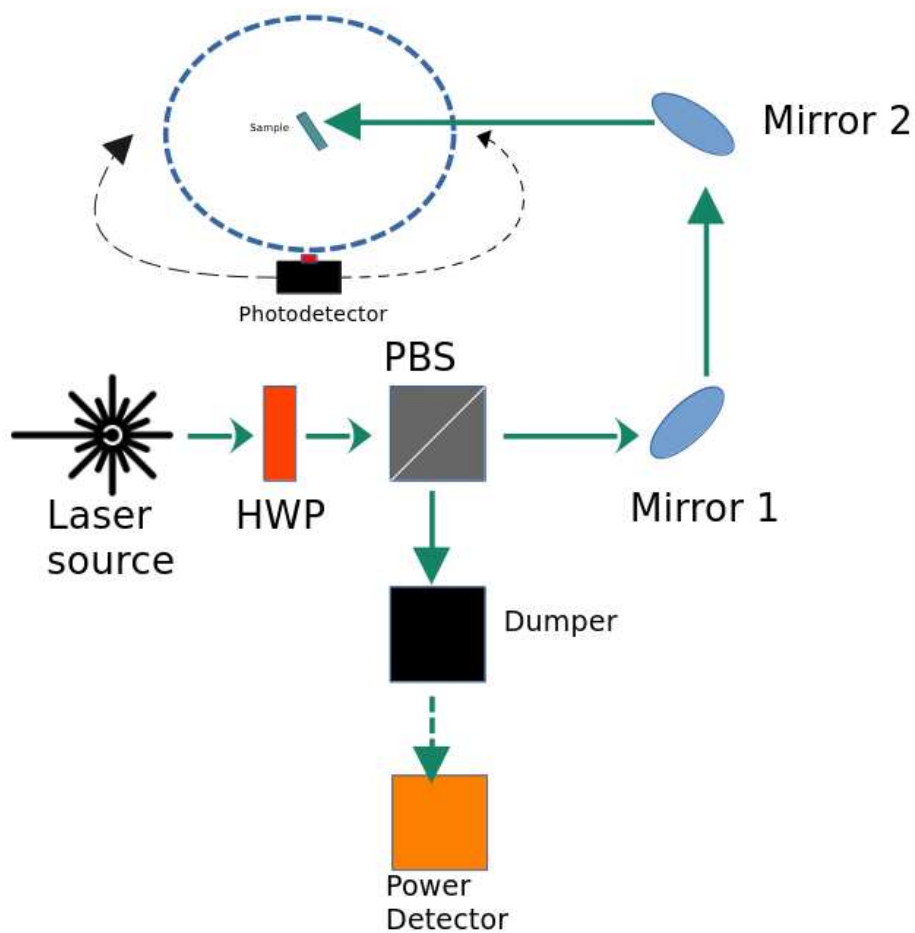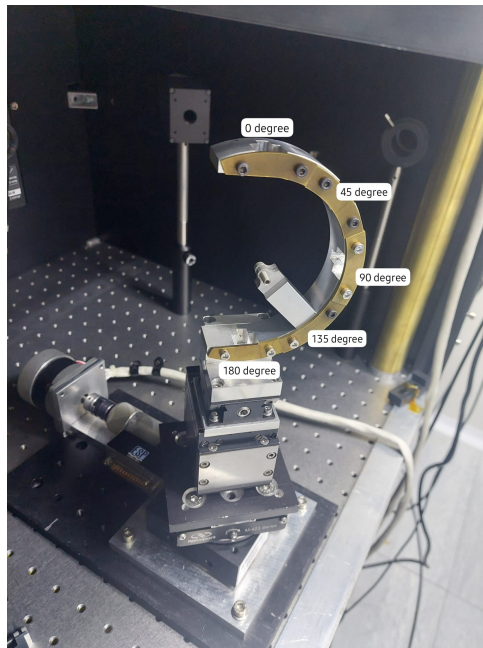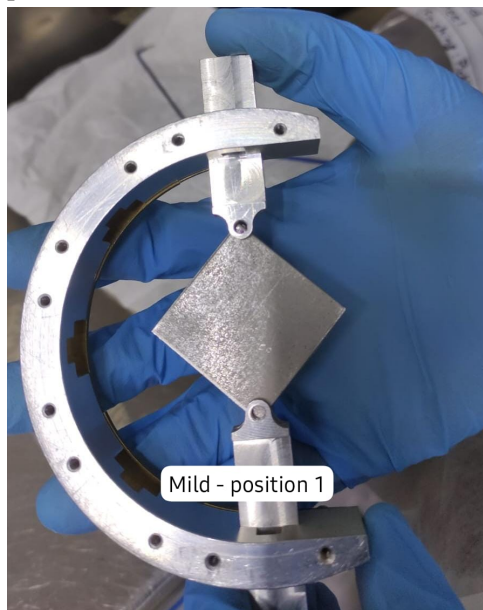

Figure 3.3: Basic schematic of the setup used to measure scattering from samples.

(a) Sample holder placed in a movable platform.

(b) Example of a metal sample fixed in the holder by using arms.
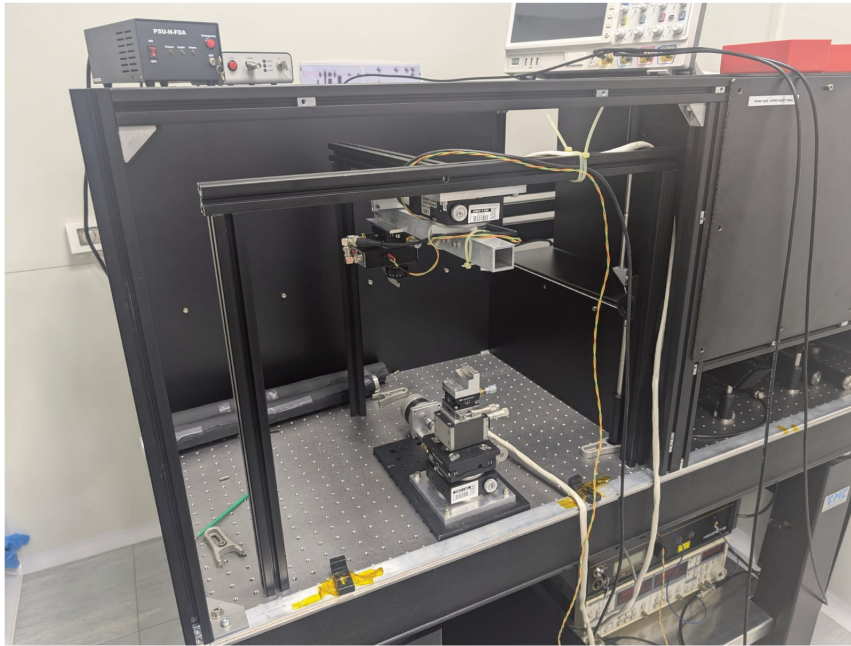
Figure 3.4

Figure 3.5: Home-build scattering machine.

During my intership, the BRDF of the background noise was measured to enhance the accuracy of the scatterometer. The result of this is presented in Figure 3.6, with the Y axis in logarithmic scale. The background signal in absence of any sample is at around 10^{-8}, which corresponds to the electrical noise or what the photodetector measures when there is no light source. At first, the results showed a pick at 40 degrees (red line). An attempt to solve the peak of scattering was to place an iris before the holder, allowing to control the beam size reaching the sample. The results shows a decrease in the scattering(Figure 3.4) when the iris aperture is smaller (green lines).
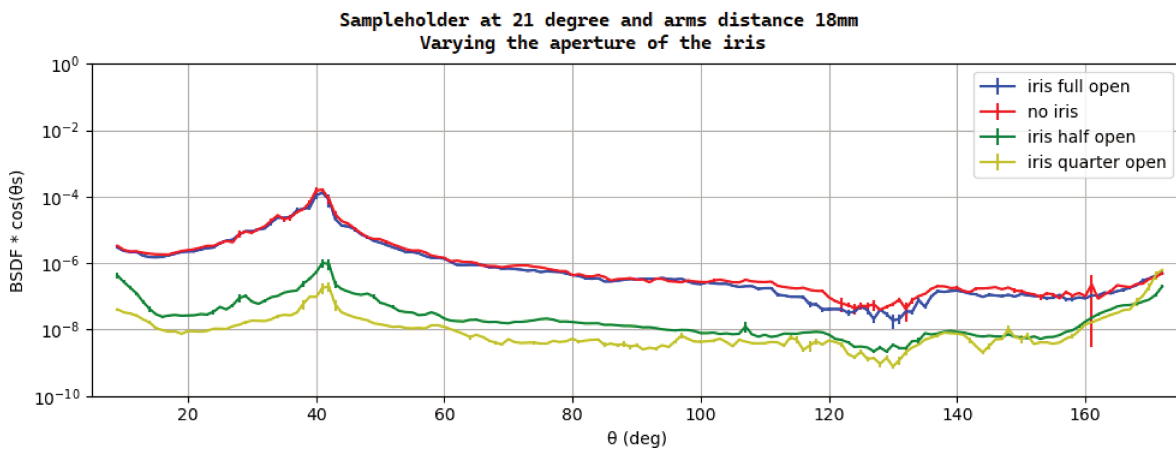

Figure 3.6: Example of the measurement of background noise.

3.4 Atomic Force Microscopy

During the early 1980s, the microstructural analysis of materials experienced a major break-through with the development of scanning probe microscopy (SPM). SPM encompasses a group of entirely analytical techniques, allowing a nanoscale spatial resolution to be determined generating three-dimensional images of a surface. SPM techniques use instruments composed primarily of a sensing probe that interacts with the surface of the sample. Feedback circuits to control the vertical position of the probe, and a computer to control scanner movements, store data, and convert data into images using specific software. The essential component of SPM is the probe, which may adopt various architectures, such as a needle-shaped metallic probe for tunneling, resulting in scanning tunneling microscopy (STM), or a probe attached to a flexible cantilever for force detection, which characterizes atomic force microscopy (AFM) [22]. AFM was developed in 1986 by Binnig, Quate, and Gerber [23] by modifying a scanning tunneling microscope, combining the apparatus with a profilometer (which quantifies roughness on a microscopic scale), thus enabling the measurement of forces in different types of materials for the analysis of metals and semiconductors or insulating surfaces.
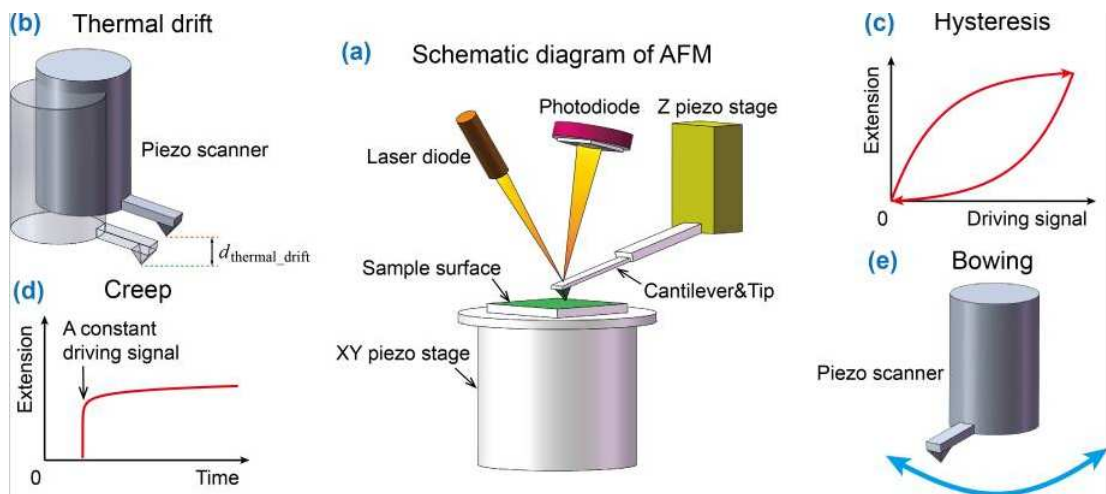

Figure 3.7: Sources of noise producing distortion in AFM. [24]

Sample images obtained from AFM can be compromised by distortion and artifacts, which are mainly caused by mechanical drift in AFM systems . A common source of noise is the drift of the tip between the movement of the XY plane and Z (height) as shown in Figure 3.7(b). Additionally, some other factors, such as hysteresis (Figure 3.7c), creep (Figure 3.7d), and bowing (Figure 3.7e) can also cause distortion and artifacts in AFM images [24]. This is why software tools are utilized to mitigate the noise effects inherent to AFM measurements.
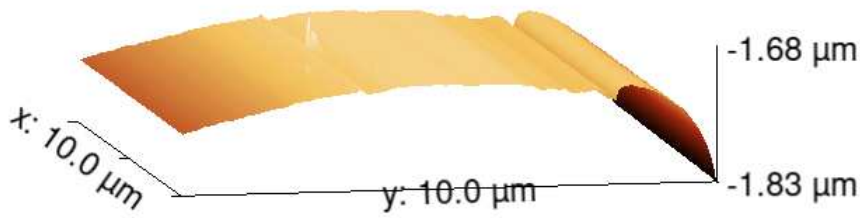
23

Figure 3.8: Raw image from sample K2 with distortion.

The AFM used to obtain 3d images of the surface from the samples K0-K5 and as deposited (sample with no annealing), is the FlexAFM (Figure 3.9) from Nanosurf [25], placed on top of an Anti-Vibration Table to reduce mechanical movements during the measurements. A single file of raw data is obtained from the AFM device software. An example of the raw data for sample K2 obtained by using AFM is shown in Figure 3.8. As previously discussed, the surface is not flat but reveals a curved surface shape and two grooves, the most pronounced on the right side. Following this, a post-processing step is performed with the software Gwyddion[26] in which a series of algorithms are used to clean and flatten the raw topographical data into a 3d image. The main algorithm used to level the raw data is named polynomial background subtraction, in which a polynomial curve determined by parameters specified manually, is fitted to the background noise and then subtracted. As a last step and using the same software, the root-mean-square (RMS) roughness values are calculated to compare the samples.
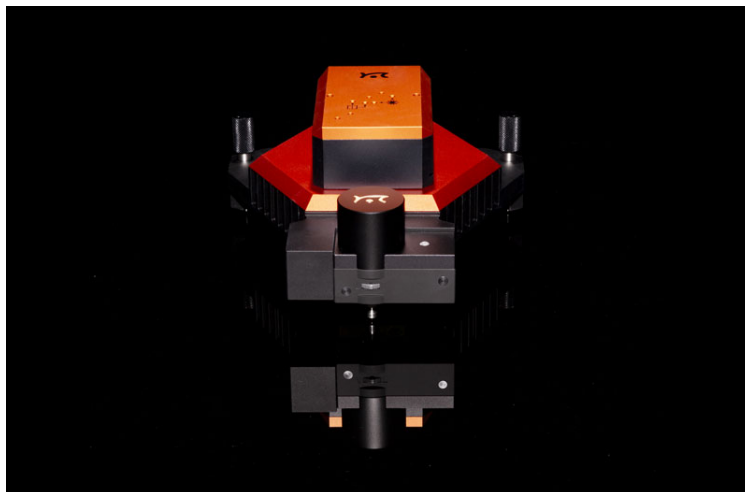

Figure 3.9: Scanning probe microscope used [25].

Chapter 4

Experimental Results and Analysis

4.1 Optical Microscopy

I used optical microscopy to take a set of 4-5 pictures at 2500x magnification for each thin film of tantalum oxide sample described in Chapter 3.1. As explained in Chapter 3.2, the polarizers were rotated until the largest quantity of grains was visible. Then, these pictures were analyzed using grain recognition software included with the microscope by first using the software to automatically select the area of as many grains as possible and then refining it by hand. Following this, a Grain Size Distribution (GSD) for each sample was obtained. This data was used in a published article [19].

The microscopy images (Figure 4.1) of the thin films samples exhibits grain structures that evolves significantly in function of annealing time. Particularly, for the as deposited and K1 samples, the surface is characterized by a uniform distribution, with no grain visible. There are no observable defects such as voids or cracks, indicative of a controlled deposition and annealing process. On the contrary, some scratches were found in some samples (Figure 4.2).
For the next samples that underwent longer annealing times, namely K1 to K5, elongated and circular-shaped grains with visible boundaries are observed, indicating the well-defined difference between individual grains and the background.

After annealing for 15 and 18 hours (samples K4 and K5), a change occurs in the positions of the grains, as they seem to be getting closer and/or on top of each other. Nevertheless, grain boundaries are still sharp.
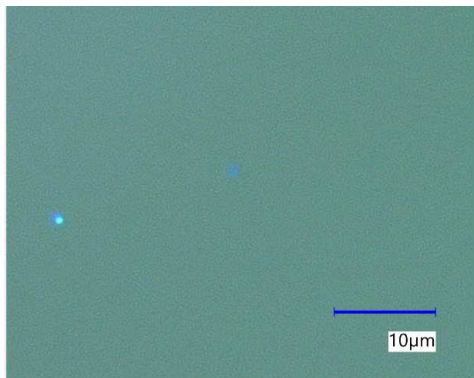As observed in Figure 3.2, these grains respond strongly to the polarization of incident light, which let us infer that they are crystals growing in the coating, since it is a typical behaviour.
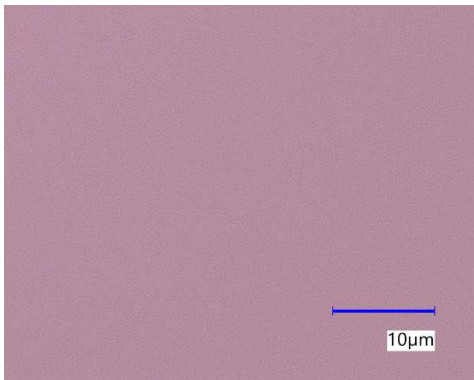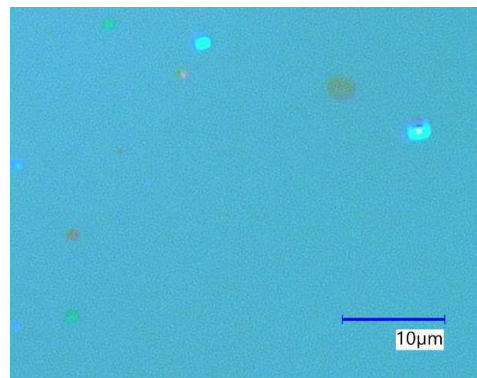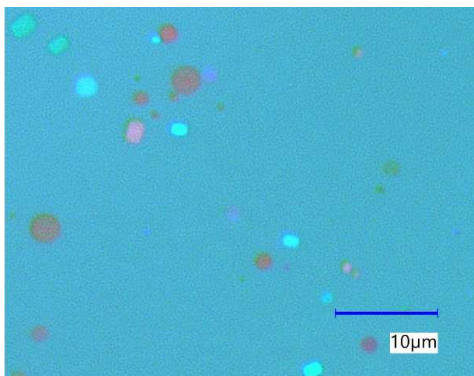
(a) Sample with no annealing.
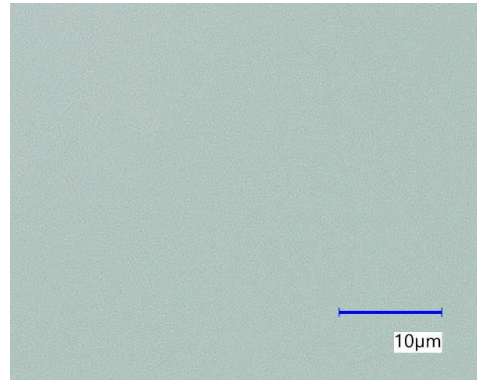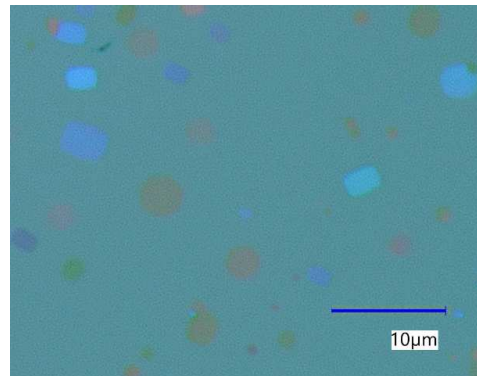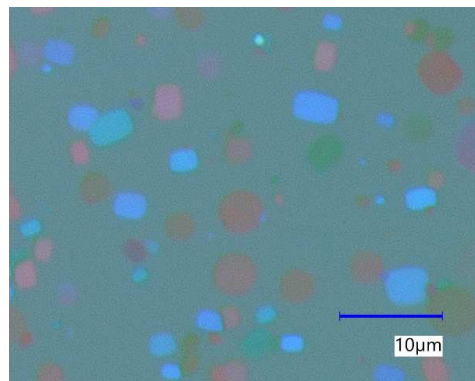

(b) K0.

(c) K1.

(d) K2.

(e) K3.

(f) K4.

(g) K5.

Figure 4.1: Images of the samples taken with the microscope at 2500x augmentation.

To quantify the crystallization process, a grain count analysis is carried out. This gave us an estimate for the crystallized fraction of the coating layer, reported in Table 4.1: the crystallized fraction is below 1% for the samples annealed for less than 9h (K1 and K2). For the following samples, this percentage grows quickly as they were treated with longer annealing times. After after carrying out a count analysis, it was also possible to estimate the grain size distribution (Figure 4.4). The grain size used is the square root of the measured grain areas reported by the software. This was done in order to remove differences due to grain shape, since they are not perfectly circular. For K1, the first but least crystallized sample, the average crystal size is already larger than the thickness of the coating film, which is around 500 nm. Therefore, crystal growth is restricted to two-dimensions since the first 630°C treatment. [19].

A plot with the average grain size for each annealing time is presented below:
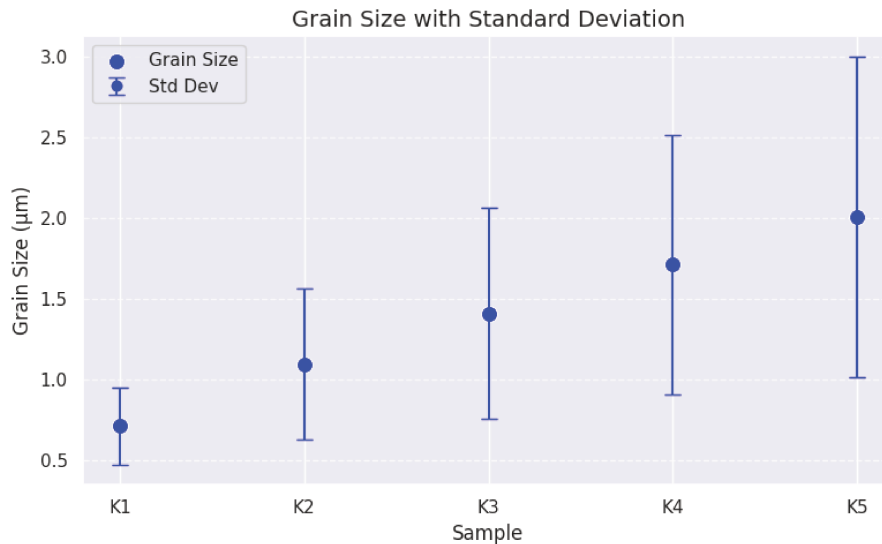
Figure 4.2: Sample average grain size.

Sample	Crystallized Fraction
K0	0%
K1	$(0.05 \pm 0.03)\%$
K2	$(0.84 \pm 0.15)\%$
K3	$(4.7 \pm 0.6)\%$
K4	$(10.3 \pm 0.6)\%$
K5	$(28.3 \pm 3.0)\%$

Table 4.1: Crystallized Fraction of K samples after annealing.
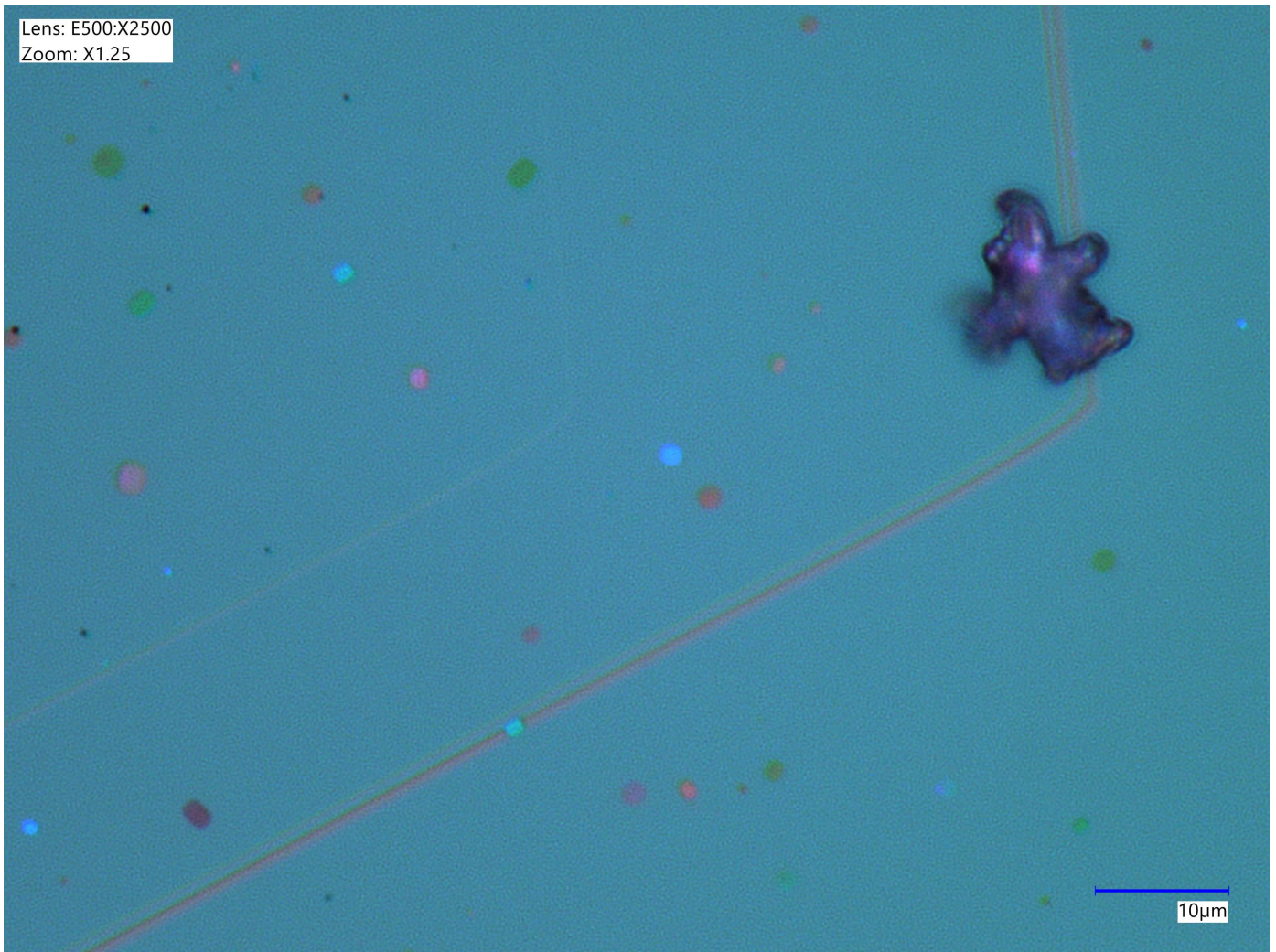
Figure 4.3: Scratch noticed in K2.

The grain size distribution of the tantalum oxide coatings was obtained to understand the effects of thermal treatments on the structure of the films. The unit of measurement used is the square root of the area reported by the microscope software.

The results revealed a variation in grain sizes across the different coating samples. At shorter annealing times, the grain size distribution exhibited a higher concentration of smaller grains. As annealing time increased, the grain size distribution shifted towards larger grains. Larger grains were observed to form more readily under prolonged thermal treatments. According to [21], the grain growth due to annealing should follow a lognormal distribution, a fitting process was carried out (Figure 4.4). Nevertheless, it did not pass a chi-squared test with one of the possible reasons that some grains are not noticeable due to different polarizations. Interestingly, the fitting approximates better to the samples with more grains (K4, K5).
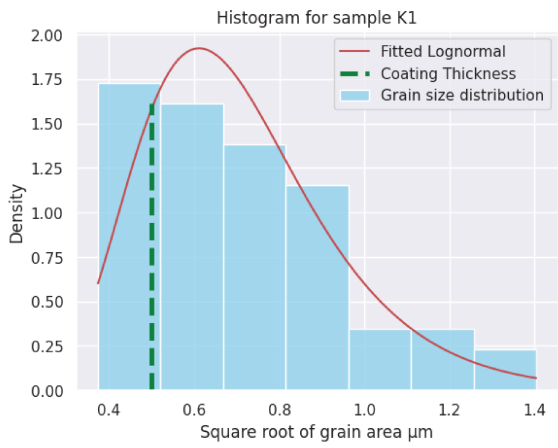
(a) Grain size distribution of K1.
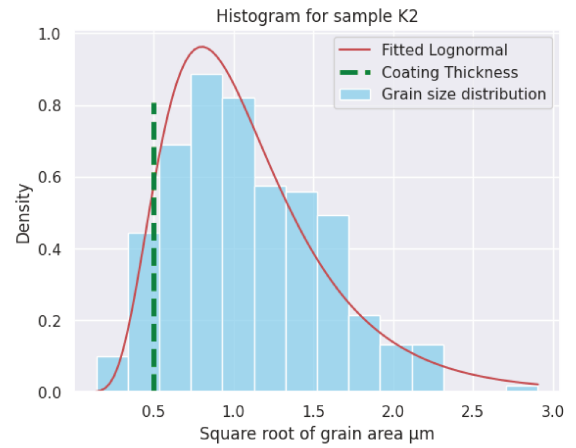
(b) Grain size distribution K2.
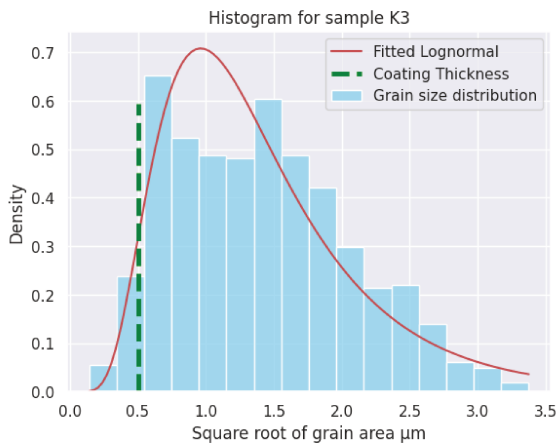
(c) Grain size distribution K3.
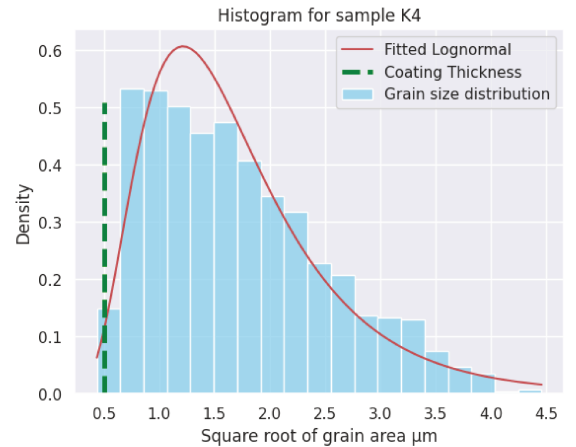
(d) Grain size distribution K4.
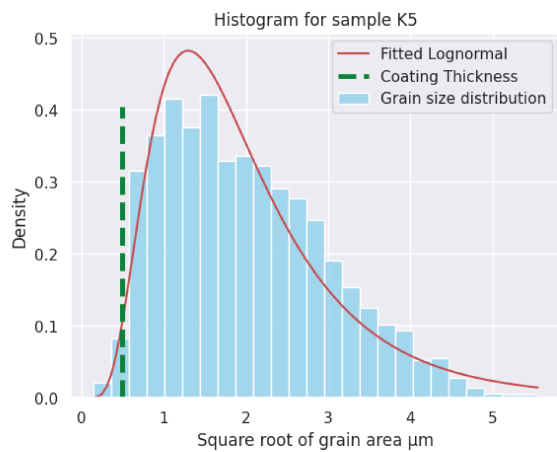
(e) Grain size distribution K5.

Figure 4.4: Grain size distribution of samples.

4.2 Scatterometer Measurement

The BRDF was estimated using a scatterometer. For each sample, measurement was done between 10 and 100 degrees, using a 532 nm laser as a light source with the sample at an incident angle of 3.3°. For the measurement between 10 and 40 degrees, an optical filter was necessarily placed in front of the photodetector to avoid saturation, as it is the range where the scattering is stronger. The expected BRDF result for the samples is an increasing scattering for the samples with a higher annealing time due to an increase in grain boundaries, number of crystalline grains and total crystallized area. However, as shown in Figure 4.5, some unexpected results are seen in the scattering behavior. The data did not follow the expected pattern. After 60 degrees, samples K0 and K1 have a similar scattering to sample K5 and k4. Samples K2, K3, K4, and K5 exhibit a consistent rate of decrease in scattering. While K0 and K1 show a constant decrease only up to 30 degrees, after this, the rate becomes smaller to the point of having a similar scattering to K5 and superior to K4.
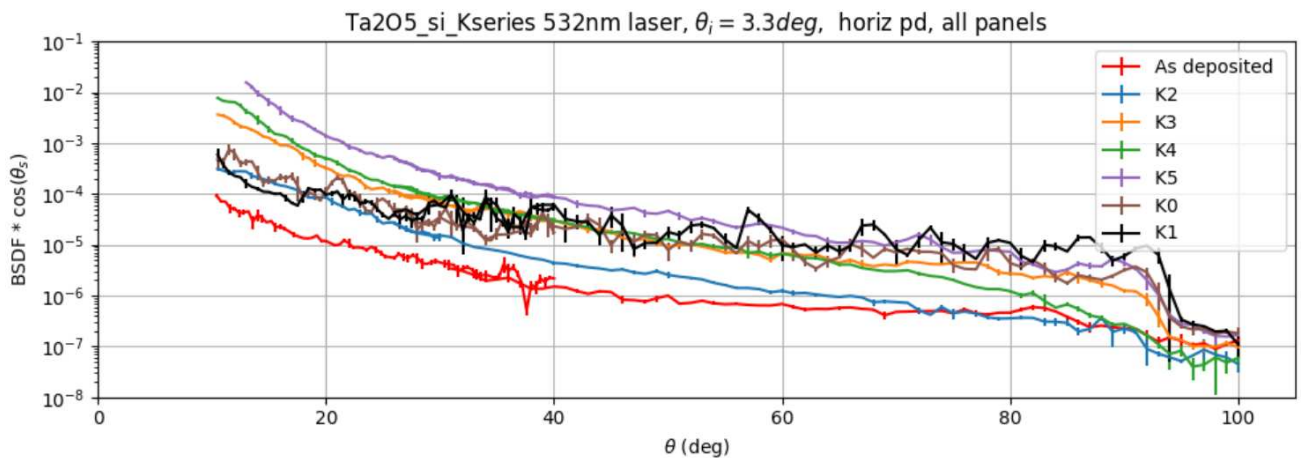
Figure 4.5: BSDF of K samples measured with the scatterometer.

It is also possible to calculate total internal scattering (TIS) by using equation 2.8 and the BRDF data measured. The results are given in Table 4.2, where an increase of TIS with respect of the annealing time is noticed between K2 and K5. As mentioned before, the BRDF measurements did not follow the expected trend from crystallization results. This is most likely caused by irregularities introducing during the handling of the samples, which complicated the direct interpretation of scattering properties.

Sample	TIS
As deposited	1.65×10^3
K0	2.408×10^{-2}
K1	9.45×10^{-3}
K2	6.67×10^{-3}
K3	4.201×10^{-2}
K4	7.117×10^{-2}
K5	1.791×10^{-1}

Table 4.2: TIS calculated from BRDF data.

4.3 Atomic Force Microscopy

(a) As deposited.

(b) K0 surface.

(c) K1 sample surface.

(d) K2 sample surface.

(e) K3 sample surface.

(f) K4 sample surface.

(g) K5 sample surface.

Figure 4.6: Some images of the samples surface taken with AFM after processing.

Using Atomic Force Microscopy (AFM), multiple images of samples K0-K5 and as-deposited were taken in an area of size $10x10\mu m$ (Figure 4.6) to investigate the surface topography.

AFM revealed changes in the surface morphology and structural properties of the sample as a function of annealing time. The images in general, appear to be almost atomically smooth, except some areas where depressions in the surface, similar in shape and dimension to the ones detected using optical microscopy, are seen.

AFM revealed changes in the surface morphology and structural properties of the sample as a function of annealing time. Some white spaces are noticed, most notable in sample K3, near the top grain. For the sample as-deposited and K0 (treated only at 500°C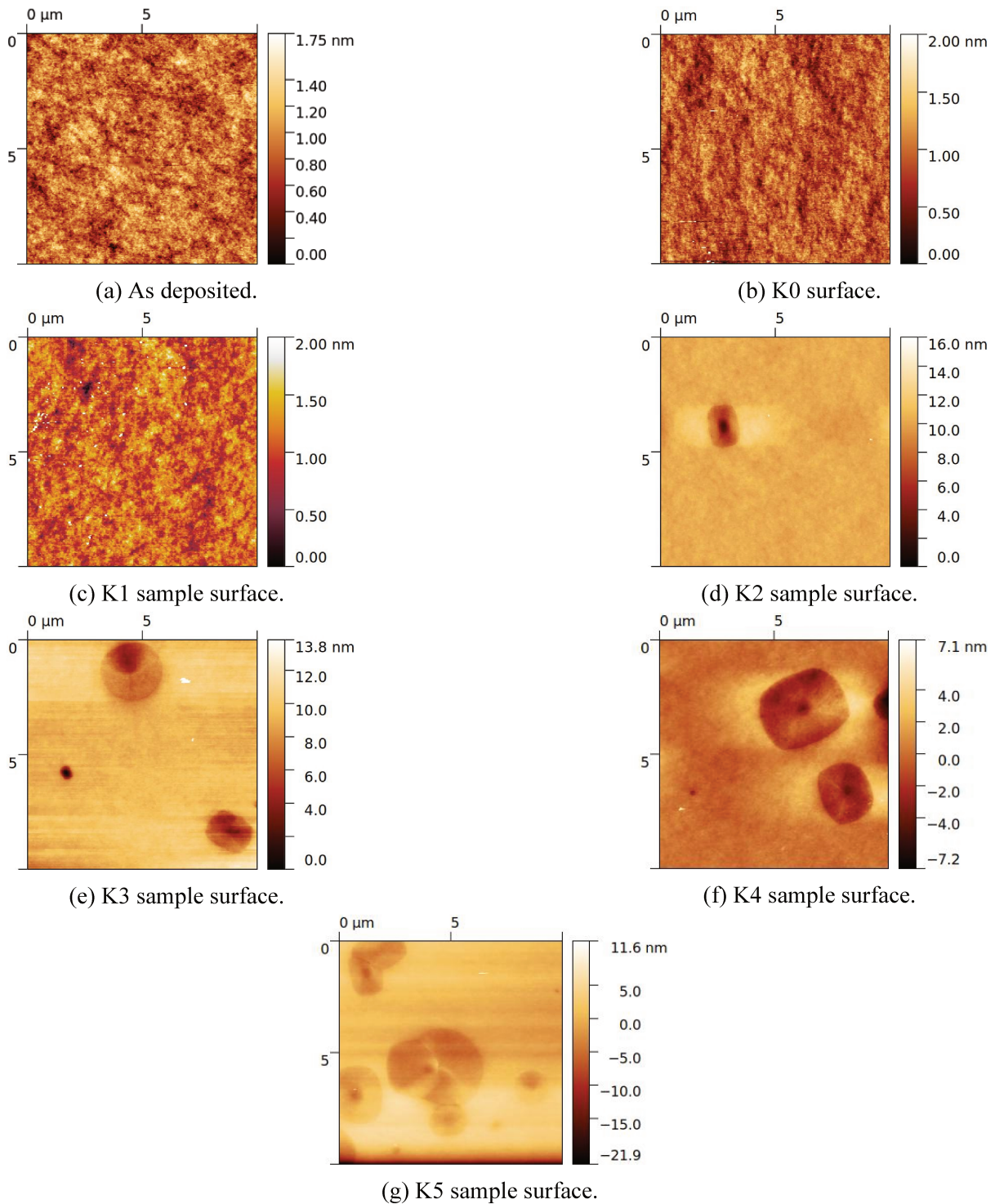), the surface presented a relatively smooth topography, with a surface roughness RMS of 0.205 nm and 0.207 nm, virtually the same. Starting at sample K1, two different roughness are calculated using the RMS method, one with the whole area and a second by 'masking' and ignoring the parts of the surface corresponding to a crystal (depression with a shape and dimension similar to what is seen using optical microscopy). For K1, a RMS roughness of 0.297 nm (full area) and 0.242 nm (masked crystals) was obtained, this is indicative of a surface that remained largely unaffected by thermal treatments. The uniformity of the surface at this stage suggests minimal transformation in the material, likely because the annealing temperature was insufficient for significant alterations.

By 9 hours of annealing (K2), the film began to show evidence of elongated and circular-shaped grains. The surface roughness correspondingly increased with it. From Figure 4.4 a clear trend in RMS is noticed, a rapid growth as function of the annealing time, indicating grains are a major source of surface roughness.
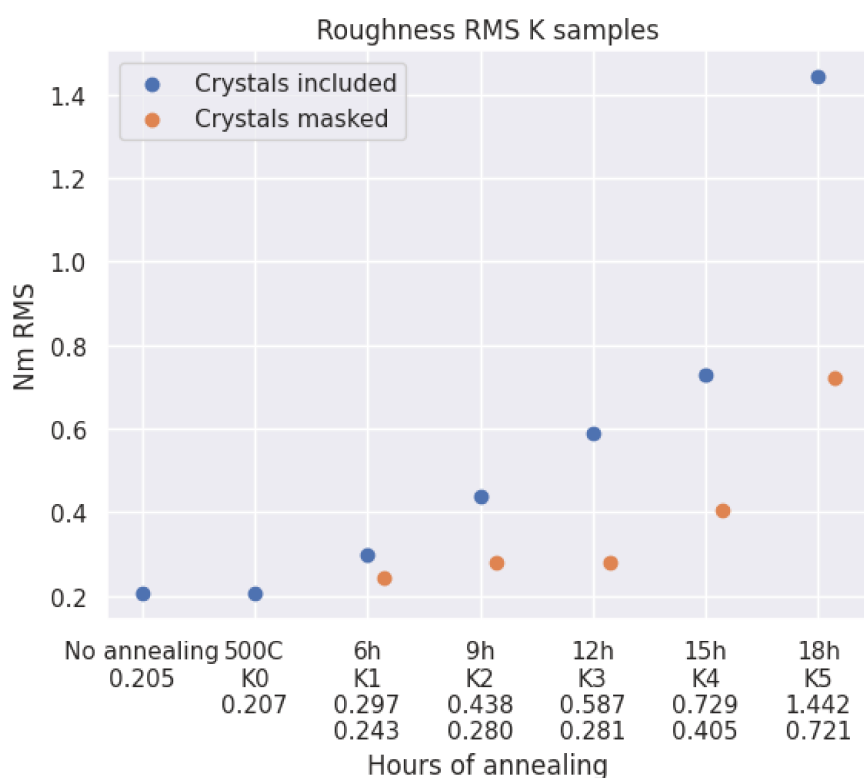
Figure 4.7: RMS calculated for K samples.

By using equation 2.9, it is possible to estimate theoretical values of TIS given the RMS obtained with AFM. The results are given in Table 4.3 assuming a 532 nm laser.

The calculated TIS increases with crystallization, however this value is far from the one obtained by using the BRDF data, leading us to believe surface scattering plays a minor role in the overall scattering of the annealed coatings.

Sample	RMS with Crystals	TIS with Crystals	RMS Crystals masked	TIS Crystal masked
As deposited	0.207nm	5×10^{-6}	-	-
K0	0.207nm	6×10^{-6}	-	-
K1	0.297nm	1.2×10^{-5}	0.243 nm	8×10^{-6}
K2	0.438nm	2.6×10^{-5}	0.280 nm	1×10^{-5}
K3	0.587nm	4.8×10^{-5}	0.281 nm	1.1×10^{-5}
K4	0.729nm	7.4×10^{-6}	0.405 nm	2.2×10^{-5}
K5	1.442nm	2.90×10^{-4}	0.721 nm	7.2×10^{-5}

Table 4.3: Theoretical TIS calculated in base of RMS of the surface.

Sample	Crystalization %	RMS from AFM (nm)	RMS from BRDF (nm)
As deposited	0%	0.205	1.72
K0	0%	0.207	6.56
K1	0.05%	0.297	4.11
K2	0.84%	0.438	3.45
K3	4.7%	0.587	8.677
K4	10.3%	0.729	11.294
K5	28.3%	1.442	17.919

Table 4.4: Surface analysis comparison.

4.4 Surface analysis comparison

A comparative study of surface roughness and crystallization characteristics was carried out using multiple methods to estimate consistency and theoretical implications. Table 4.4 summarizes the results, comparing crystallization data with the sample's surface roughness parameter obtained from two distinct approaches: roughness derived from atomic force microscopy (AFM) data, and roughness values calculated by integrating the bidirectional reflectance distribution function (BRDF) to derive the TIS using Equation 2.10.

Crystallization provides an indirect indicator of the surface structure modifications due to annealing, we expect an increment of the sample roughness as crystallization increases. RMS roughness values calculated by using Equation 2.10 showed a major difference between the RMS roughness obtained from AFM. These findings underline that surface roughness does not completely explain the changes in optical scatter due to annealing and that the grains in the material play an important role in it.

Chapter 5

Conclusions

In this thesis, we have investigated the optical and surface changes of tantalum oxide coatings samples that underwent different annealing times. These changes were measured by calculating and analyzing their Bidirectional Reflectance Distribution Function (BRDF) and surface roughness. The objective of this research was to gain an understanding of the relation between the coating structure and their optical performance, which is necessary for improving the mirrors in Gravitational Wave (GW) detectors.

Summary of Findings : The BRDF measurements of the thin film samples revealed variations in the scattering behavior, which is significantly influenced by the microstructural properties of the films. In particular, BRDF and TIS was found to be strongly dependent on the grain distribution and the roughness of the surface, and in consequence, to the annealing time. These findings shows the impact of the thermal treatment time on the scattering of light.

Roughness measurements, obtained through Atomic Force Microscopy (AFM), confirmed that the samples exhibited an increase in its roughness, from relatively smooth up to K3, and a rapid increase for K4 and K5. The RMS roughness was quantified, showing a mild relationship between surface roughness and the optical scattering behavior. However, there is a direct relation between roughness levels and crystallization.

The insights gained from this work contribute to the understanding of tantalium oxide characterization, providing a more nuanced understanding of how surface roughness and grain distribution influences its optical properties.

Outlook : While this study has provided valuable insights into the relationship between thermal treatment of the coating and its scattering, further research could be used to improve the precision and reliability of the measurements conducted in this study. In the case of optical microscopy, while it allow us to visualize grain structures, it can face limitations when grains are

not consistently visible under some polarization conditions. As observed in this thesis (Figure 3.2), some grains are not noticeable due to variations in their orientation or optical properties under different polarizations. This has a direct impact to the accuracy of the grain size distribution analysis, as certain grains may be omitted or mischaracterized. To address this issue, utilizing a more advanced computer vision solutions to merge images captured under different polarization angles could significantly enhance the visibility of all grains within the sample. Such software could combine multiple images taken under different polarizations, into a single composite, where grains are clearly delineated regardless of its orientation.

During the imaging process using optical microscopy and Atomic Force Microscopy (AFM), some scratches were spotted on the surface of the samples (Figure 4.3). These imperfections may have influenced the accuracy of the BRDF measurements, as the surface irregularities could lead to scattering distortions in the reflectance data. Therefore, the BRDF distribution obtained in this study was not as clear or reliable as desired. To improve the quality of future measurements, more careful handling of the samples is necessary. This includes taking extra precautions during handling and imaging to prevent or reduce the probabilty of surface damage. Employing more precise methods for mounting and securing the samples, as well as using protective handling tools, could significantly reduce the occurrence of damage at the surface of the coating.

Acknowledgement

I would like to express my most profound gratitude to my family for their unwavering support, love, and encouragement throughout my studies. Their belief in me has been my foundation and source of inspiration providing strength during difficult times and celebrating every small victory along the way. Without their sacrifices and constant reassurance, this achievement would not have been possible.

I am also profoundly grateful to professor Marco Bazzan and Dr. Valeria Milotti for giving me the opportunity to do my thesis them and also to my colleagues at the lab for their collaboration, guidance, and the opportunity to learn from each one of you. The dynamic teamwork and stimulating discussions we shared have been instrumental in shaping my understanding and perspective, helping me grow both as a researcher and as an individual.

To my friends, I am profoundly thankful for your constant motivation, patience, and understanding. Your ability to lift my spirits, lend an ear, and inspire me to persevere has made this journey not only bearable but truly meaningful. The memories we have shared during this time will remain invaluable to me.

Bibliography

[1] I. Newton, *Philosophiae naturalis principia mathematica*. Jussu Societatis Regiae ac Typis Josephi Streater. Prostat Venales apud Sam. Smith ad insigna Principis Walliae in Coemiterio D. Pauli, aliosq, nonnullos Bibliopolas, 1687. [Online]. Available: `https://books.google.it/books?id=-dVKAQAAIAAJ`.

[2] H. Poincaré, "On the dynamics of the electron (english translation by Scott Walter)," *Rendiconti del Circolo Matematico di Palermo*, vol. 21, pp. 129–176, 1906. [Online]. Available: `http://www.univ-nancy2.fr/poincare/bhp/pdf/hp1906rpen.pdf`.

[3] A. Einstein, "Näherungsweise Integration der Feldgleichungen der Gravitation," *Sitzungsberichte der Königlich Preussischen Akademie der Wissenschaften*, pp. 688–696, Jan. 1916.

[4] B. C. Barish, *The detection of gravitational waves with ligo*, 1999. arXiv: `gr-qc/9905026 [gr-qc]`.

[5] S. Dhurandhar and S. Mitra, *General Relativity and Gravitational Waves: Essentials of Theory and Practice*. Springer International Publishing, 2022, isbn: 9783030923358. doi: `10.1007/978-3-030-92335-8`. [Online]. Available: `http://dx.doi.org/10.1007/978-3-030-92335-8`.

[6] J. Cervantes-Cota, S. Galindo-Uribarri, and G. Smoot, "A brief history of gravitational waves," *Universe*, vol. 2, no. 3, p. 22, Sep. 2016, issn: 2218-1997. doi: `10.3390/universe2030022`. [Online]. Available: `http://dx.doi.org/10.3390/universe2030022`.

[7] I. CiteDrive, *Gravitational-wave candidate event database (gracedb)*, `https://gracedb.ligo.org/latest/` [Accessed: (16-11-2024)], 2024.

[8] V. P. M.E. Gertsenshtein, "On the detection of low-frequency gravitational waves," *Soviet Journal of Experimental and Theoretical Physics*, vol. 16, p. 433, 1962.

[9] B. P. Abbott, R Abbott, R Adhikari, *et al.*, "Ligo: The laser interferometer gravitational-wave observatory," *Reports on Progress in Physics*, vol. 72, no. 7, p. 076 901, Jun. 2009, issn: 1361-6633. doi: `10.1088/0034-4885/72/7/076901`. [Online]. Available: `http://dx.doi.org/10.1088/0034-4885/72/7/076901`.

[10] D. Bersanetti, B. Patricelli, O. J. Piccinni, F. Piergiovanni, F. Salemi, and V. Sequino, "Advanced Virgo: Status of the detector, latest results and future prospects," *Universe*, vol. 7, no. 9, p. 322, Aug. 2021, issn: 2218-1997. doi: `10.3390/universe7090322`. [Online]. Available: `http://dx.doi.org/10.3390/universe7090322`.

[11] T. V. Collaboration, "Advanced virgo technical design report," Tech. Rep., 2012, `https://tds.virgo-gw.eu/?content=3&r=9317` [Accessed: (16-11-2024)].

[12] B. Gao, J. P. George, J. Beeckman, and K. Neyts, "Design, fabrication and characterization of a distributed bragg reflector for reducing the étendue of a wavelength converting system," *Opt. Express*, vol. 28, no. 9, pp. 12 837–12 846, 2020. doi: `10.1364/OE.391080`. [Online]. Available: `https://opg.optica.org/oe/abstract.cfm?URI=oe-28-9-12837`.

[13] R. Paschotta, *Bragg mirrors*, RP Photonics Encyclopedia. [Online]. Available: `https://www.rp-photonics.com/bragg_mirrors.html` (visited on 11/13/2024).

[14] B. P. Kafle, *Chemical Analysis and Material Characterization by Spectrophotometry*. Elsevier, 2020;2019, isbn: 9780128148662; 0128148667. [Online]. Available: `libgen.li/file.php?md5=64355f855cc003a189939ec4b73c554d`.

[15] E. Fest, *Stray light analysis and control* (Press Monographs). Bellingham, WA: SPIE Press, Apr. 2013.

[16] A. Manallah and M. Bouafia, "Application of the technique of total integrated scattering of light for micro-roughness evaluation of polished surfaces," *Physics Procedia*, vol. 21, pp. 174–179, 2011, issn: 1875-3892. doi: `10.1016/j.phpro.2011.10.026`. [Online]. Available: `http://dx.doi.org/10.1016/j.phpro.2011.10.026`.

[17] I. T. Schmiegelow, "Characterizing light scattering sources in gravitational-wave interferometers," M.S. thesis, University of Padova, 2022/2023.

[18] *Laboratoire des materiaux avances*. [Online]. Available: `lma.in2p3.fr`.

[19] G. Favaro, V. Milotti, D. Alonso Diaz Riega, *et al.*, "Reduction of mechanical losses in ion-beam sputtered tantalum oxide thin films via partial crystallization," *Classical and Quantum Gravity*, vol. 41, no. 10, p. 105 009, Apr. 2024, issn: 1361-6382. doi: `10.1088/1361-6382/ad3c8a`. [Online]. Available: `http://dx.doi.org/10.1088/1361-6382/ad3c8a`.

[20] G. Favaro, "Crystallization of amorphous tantala coatings and its implication on gw interferometry," Ph.D. dissertation, University of Padova, 2024.

[21] A. V. Teran, A. Bill, and R. B. Bergmann, "Time-evolution of grain size distributions in random nucleation and growth crystallization processes," *Physical Review B*, vol. 81, no. 7, Feb. 2010, issn: 1550-235X. doi: `10.1103/physrevb.81.075319`. [Online]. Available: `http://dx.doi.org/10.1103/PhysRevB.81.075319`.

[22] R. Tararam, P. S. Garcia, D. K. Deda, J. A. Varela, and F. de Lima Leite, "Atomic force microscopy: A powerful tool for electrical characterization," in *Nanocharacterization Techniques*. Elsevier, 2017, pp. 37–64, isbn: 9780323497787. doi: `10.1016/b978-0-323-49778-7.00002-3`. [Online]. Available: `http://dx.doi.org/10.1016/B978-0-323-49778-7.00002-3`.

[23] G. Binnig, C. F. Quate, and C. Gerber, "Atomic force microscope," *Phys. Rev. Lett.*, vol. 56, pp. 930–933, 9 1986. doi: `10.1103/PhysRevLett.56.930`. [Online]. Available: `https://link.aps.org/doi/10.1103/PhysRevLett.56.930`.

[24] Y. Wang, T. Lu, X. Li, and H. Wang, "Automated image segmentation-assisted flattening of atomic force microscopy images," *Beilstein Journal of Nanotechnology*, vol. 9, pp. 975–985, Mar. 2018, issn: 2190-4286. doi: `10.3762/bjnano.9.91`. [Online]. Available: `http://dx.doi.org/10.3762/bjnano.9.91`.

[25] *Flexafm*, `www.nanosurf.com`, Accessed: 2024-10-20.

[26] D. Nečas and P. Klapetek, "Gwyddion: An open-source software for SPM data analysis," *Central European Journal of Physics*, vol. 10, pp. 181–188, 1 2012, issn: 1895-1082. doi: `10.2478/s11534-011-0096-2`. [Online]. Available: `http://gwyddion.net/`.